Materials Advances

ROYAL SOCIETY OF CHEMISTRY

PAPER

View Article Online
View Journal | View Issue

Cite this: *Mater. Adv.*, 2026, 7, 4811

A microneedle with a photoactive electrospun backing layer enables multitherapy and combined drug delivery to the skin wound

Maryam Toolabi,[abc] Yuewen Zhu,[d] Mahsa Akbari,[ab] Mohammad Reza Eskandari,[c] Narges Forouzideh,[a] Hélder A. Santos *[d] and Mohammad-Ali Shahbazi *[d]

Skin wound healing is frequently impaired by infection, inflammation, insufficient vascularization, and chronic pathological conditions, highlighting the need for therapeutic strategies that can address multiple barriers simultaneously. In this study, we developed a hybrid wound-healing platform that integrates dissolvable microneedles (MNs) with a photoactive electrospun backing layer to enable sequential and complementary therapeutic functions. The electrospun scaffold (PGTBi), composed of poly(vinyl alcohol) and gelatin and loaded with taurine (Tau) and bismuth sulfide nanorods (Bi_2S_3 NRs), was fabricated to provide an extracellular matrix-mimicking dressing with optional near-infrared (NIR)-responsive photothermal activity. The dissolvable MNs (PHA), composed of poly(methyl vinyl ether-*alt*-maleic acid) and hyaluronic acid and loaded with allantoin, were designed for rapid intratissue delivery following application to the wound bed. Upon insertion, the MNs dissolved within minutes, potentially enabling rapid exposure of allantoin within the wound tissue, while the electrospun PGTBi layer remained adhered to the wound surface, serving as a regenerative dressing and a secondary reservoir for bioactive components. The physicochemical properties, mechanical performance, dissolution behavior, photothermal response, antibacterial activity, and biocompatibility of the system were systematically evaluated *in vitro*. *In vivo* wound-healing efficacy showed significantly enhanced wound closure, improved re-epithelialization, and increased collagen deposition compared to control and non-irradiated groups. Histological and biochemical analyses confirmed good biocompatibility and the absence of systemic toxicity. Overall, this study demonstrates the feasibility of a hybrid dissolvable MN-electrospun platform that provides rapid intratissue delivery combined with a surface-level reservoir of a therapeutic drug and optional photothermal activation, offering a promising approach for accelerated wound healing.

Received 7th November 2025,
Accepted 27th March 2026

DOI: 10.1039/d5ma01289a

rsc.li/materials-advances

1. Introduction

The skin, the largest multilayered organ of the human body, serves as a dynamic barrier that preserves homeostasis and protects against microbial invasion.[1,2] When this barrier is disrupted by wounds, the resulting injury imposes a significant global healthcare burden,[3] in which its healing is a highly coordinated physiological process encompassing hemostasis, inflammation, proliferation, and tissue remodeling.[4] Although this process occurs naturally, it can be severely impaired by poor vascularization, inflammation, chronic diseases, or aging.[5] These multifactorial challenges indicate that no single therapeutic approach can fully restore normal healing, underscoring the need for multimodal and synergistic therapies to promote tissue regeneration.

In this context, electrospun nanofibers have attracted considerable attention as wound dressing materials owing to the possibility of making them multifunctional while presenting high porosity, large surface-to-volume ratio, and extracellular matrix (ECM)-mimicking architecture, which collectively support cell adhesion, migration, and proliferation.[5–7] Electrospinning offers a versatile and cost-effective technique for fabricating polymeric nanofibers with tunable compositions and structures.[8] Recent studies have further demonstrated the potential of ECM-like electrospun scaffolds loaded with bioactive molecules, antioxidants, or antibacterial agents to modulate

[a] *Department of Pharmaceutical Nanotechnology, School of Pharmacy, Zanjan University of Medical Sciences, 45139-56184 Zanjan, Iran*
[b] *Zanjan Pharmaceutical Nanotechnology Center, Zanjan University of Medical Sciences, Zanjan, Iran*
[c] *Department of Pharmacology and Toxicology, School of Pharmacy, Zanjan University of Medical Science, 45139-56184 Zanjan, Iran*
[d] *Department of Biomaterials and Biomedical Technology, The Personalized Medicine Research Institute (PRECISION), University Medical Center Groningen (UMCG), University of Groningen, Antonius Deusinglaan 1, 9713 AV, Groningen, Netherlands. E-mail: h.a.santo@umcg.nl, m.a.shahbazi@umcg.nl*

inflammation and enhance tissue regeneration.[9,10] However, electrospun nanofibers primarily act at the wound surface, and their therapeutic efficacy is often limited by poor penetration into deeper wound tissue, the presence of necrotic debris in the interface, and diffusion-controlled drug release kinetics, which may delay early-stage healing.[11] Therefore, there is growing demand for wound dressings that can address these challenges.

To overcome these limitations, dissolvable microneedles (MNs) have emerged as minimally invasive delivery systems capable of transporting therapeutic agents across the stratum corneum into deeper skin layers.[12] Recent advances have shown that dissolvable MNs can enhance localized drug bioavailability, stimulate angiogenesis, and accelerate re-epithelialization in acute and chronic wounds.[13–15] Nevertheless, the restricted internal volume of MN tips significantly limits drug-loading capacity, making it challenging to deliver high doses or multiple therapeutics required for complex wound environments, particularly in infected or chronic wounds.

To address these challenges, several recent studies have explored hybrid platforms combining MNs with secondary wound dressings, nanofibrous layers, or loading drug molecules in the backing layer of MNs.[16–18] While these systems demonstrate improved wound coverage and drug delivery, most rely on passive release mechanisms and lack external stimulation or spatiotemporally controlled therapy. Moreover, integration of photothermal therapy (PTT) into such hybrid MN-nanofiber systems remains largely unexplored.

This approach has recently emerged as an attractive, antibiotic-free strategy for suppressing bacterial infection, known as one of the most critical complications that delays wound healing and increases the risk of chronic inflammation.[19,20] Under near-infrared (NIR) irradiation (700–1100 nm), photothermal agents convert light into localized heat, which can effectively disrupt bacterial membranes at temperatures of ~ 50 °C, while at mild hyperthermic temperatures (38–41 °C) they can stimulate angiogenesis and fibroblast activity.[21–23] Despite promising results, most reported PTT-based wound dressings are limited to surface-applied films or hydrogels and lack the ability to deliver therapeutics into deeper wound tissue. In addition, this approach is a suitable alternative to conventional antibiotics[19] due to its broad spectrum, noninvasiveness, and lack of resistance development.[24–26]

Herein, we report a multifunctional hybrid platform that uniquely integrates dissolvable MNs with a photoactive electrospun backing layer, enabling spatially and temporally controlled multitherapy for wound healing. In this system, a poly(vinyl alcohol) (PVA) and gelatin (Gela) electrospun nanofibrous scaffold that is loaded with Tau and bismuth sulfide nanorods, named PGTBi, is merged with dissolvable MNs composed of poly(methyl vinyl ether-*alt*-maleic acid) (PMVE-MA), hyaluronic acid (HA), and allantoin (PHA). This design aims to address key limitations of existing platforms by combining (i) microneedle-assisted intratissue rapid dissolution, (ii) surface-level therapeutic support from ECM-mimicking nanofibers, and (iii) on-demand NIR-triggered photothermal antibacterial and regenerative stimulation.

Bismuth sulfide nanorods (Bi_2S_3 NRs) were selected as photothermal agents due to their strong NIR absorption, excellent photothermal conversion efficiency, and favorable biocompatibility.[27–29] To ensure homogeneous dispersion, polyvinylpyrrolidone (PVP) was used as a non-toxic stabilizer.[30] The electrospun PGTBi backing layer, composed of poly(vinyl alcohol) (PVA) and gelatin (Gela), provides structural integrity, moisture retention, and ECM-like biochemical cues, while Tau contributes antioxidant and anti-inflammatory effects.[31–33] The dissolvable MN arrays, called PHA, were made of poly methyl vinyl ether-*alt*-maleic acid (PMVE-MA) and hyaluronic acid (HA), loaded with allantoin (Alla). Alla supports wound repair through its antioxidant and fibroblast proliferation effects,[34,35] while HA can facilitate cell proliferation and ECM organization.[36]

Compared with recent MN-based or electrospun wound-healing platforms, this hybrid PGTBi-PHA system offers a distinct advantage by enabling multistage, multimodal therapy through the combined delivery of therapeutics mediated by needles of the MNs and the electrospun backing layer, along with externally triggered photothermal activation. Upon application to the wound bed, the MNs dissolve within minutes to deliver therapeutics into deep tissue, while the photoactive electrospun layer remains adhered to the wound surface, functioning as both a regenerative dressing and a secondary drug depot. This integrated strategy overcomes the intrinsic limitations of conventional MNs and surface dressings, offering a promising and versatile solution for accelerated wound healing, infection control, and tissue regeneration.

2. Results and discussion

2.1. Synthesis and characteristics of Bi_2S_3 NRs

To demonstrate the successful synthesis of Bi_2S_3 NRs, photographs of the synthesis medium were taken, showing the color change of the $Bi(NO_3)_3{\cdot}5H_2O$ solution from white to black-brown after adding thioacetamide solution (Fig. 1a). The size and morphology of the prepared Bi_2S_3 NRs were investigated by transmission electron microscopy (TEM), showing a rod-shaped structure (Fig. 1b) with average lengths and widths of 75 and 22 nm, respectively (Fig. 1c and d). Fig. 1e shows that the zeta potential of Bi_2S_3 NRs is -20.97 ± 0.4 mV. Energy-dispersive X-ray (EDX) spectrum analysis confirmed that only Bi and S elements were detected in Bi_2S_3 NRs, and the mapping images showed a uniform distribution of Bi and S elements (Fig. 1f).

The NIR absorption spectrum of an aqueous dispersion containing Bi_2S_3 NRs exhibited strong light absorbance in the 700–900 nm wavelength range, attributable to their narrow bandgap of 1.3 eV, a characteristic feature of semiconductor materials (Fig. 1g).[37–39] Additionally, the absorbance increased with the increasing concentration of Bi_2S_3 NRs, indicating concentration-dependent light absorption and good dispersion of the Bi_2S_3 NRs in water. This property makes Bi_2S_3 NRs particularly promising for applications such as photothermal conversion in local therapies, where efficient NIR light absorption can generate localized heat to combat issues like bacterial infections in wound beds.

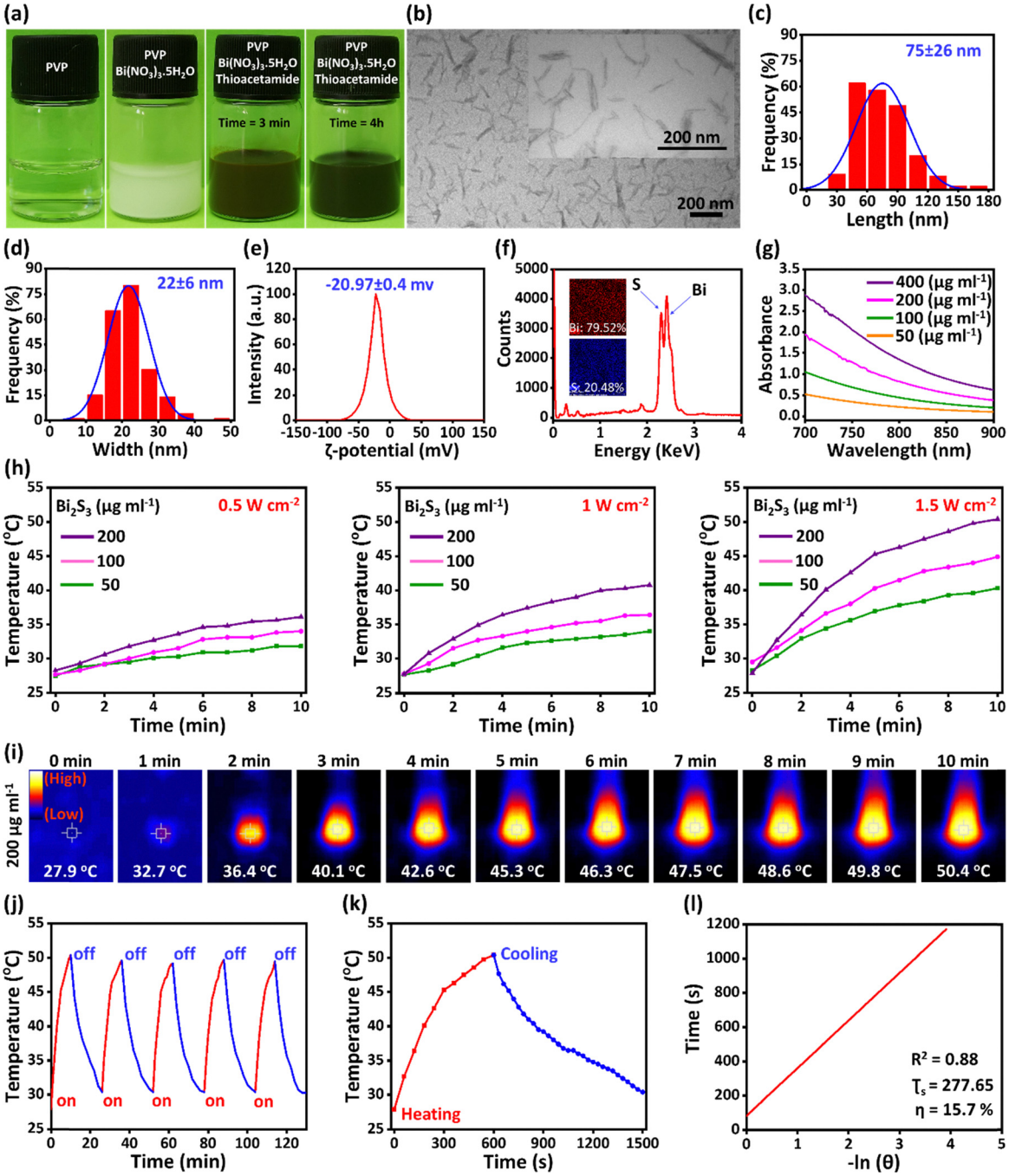

Fig. 1 Characterization of Bi_2S_3 NRs. (a) Photographs of the synthesis steps of Bi_2S_3 NRs over 4 h. (b) TEM image of Bi_2S_3 NRs. (c and d) Size distribution of Bi_2S_3 NRs. (e) Zeta potential of Bi_2S_3 NRs. (f) EDX analysis of Bi_2S_3 NRs. (g) NIR absorbance spectra of Bi_2S_3 NRs. (h) Photothermal curves of different concentrations of Bi_2S_3 NRs under an 808 nm laser (1.5 W cm^{-2}). (i) Infrared thermal photographs of Bi_2S_3 NRs under 10 min light irradiation (808 nm) with a power density of 1.5 W cm^{-2}. (j) Photostability of Bi_2S_3 NRs. (k) Photothermal diagram of the aqueous dispersion of Bi_2S_3 NRs (200 μg ml^{-1}) under an 808 nm laser irradiation (1.5 W cm^{-2}) for 10 min, followed by a 15 min cooling phase. (l) Plot of cooling time *versus* $-\ln\theta$ obtained from the cooling phase of figure k.

2.2. *In vitro* photothermal performance

To evaluate the photothermal effect, the aqueous dispersions of Bi_2S_3 NRs in different concentrations (50, 100, and 200 μg ml^{-1}) were exposed to an 808 nm laser with different power densities (0.5, 1, and 1.5 W cm^{-2}) for 10 min. After irradiation with the NIR laser, the temperature of the Bi_2S_3 NR suspensions increased rapidly with the increase in irradiation time, concentration, and laser power density (Fig. 1h). After 10 min NIR light irradiation with a power density of 1.5 W cm^{-2}, the temperature of the Bi_2S_3 NRs with concentrations of 50, 100, and 200 μg ml^{-1} increased to 40.3, 44.9, and 50.4 °C, respectively (Fig. S1). The heat generation trend with an 808 nm laser (power density

1.5 W cm^{-2}) was recorded every 1 min using an IR thermal imaging camera (Fig. 1i). Based on these results and considering that most bacteria are destroyed at 50 °C,[40] the concentration of 200 μg ml^{-1} of Bi_2S_3 NRs and the NIR power of 1.5 W cm^{-2} were selected as a potential antibacterial agent for wound healing studies.

Considering the importance of photostability for long-term antimicrobial activity,[41] the samples were exposed to NIR light in several intervals to evaluate stable heat generation. As shown in Fig. 1j, no obvious decrease in the temperature of Bi_2S_3 NRs was observed after 5 cycles of laser irradiation, indicating the good photostability and reusability of Bi_2S_3 NRs for multiple local therapies. To calculate the photothermal conversion efficiency (η), 1 ml of an aqueous dispersion of Bi_2S_3 NRs (200 μg ml^{-1}) was irradiated by an 808 nm laser (1.5 W cm^{-2}) for 10 min and then cooled naturally (Fig. 1k). Using the obtained heating–cooling graph, the photothermal conversion efficiency of the Bi_2S_3 NRs was calculated to be 15.7% (Fig. 1l; see the SI for details).[42–44] This result confirms the PTT effect of the Bi_2S_3 NRs, which is employed for wound healing in this study.

2.3. Physicochemical characterization of Tau and Bi_2S_3 NR-loaded nanofibers

The electrospinning process was successfully used to prepare nanofibrous patches of PG (PVA + Gela), PGT (PVA + Gela + Tau), PGBi (PVA + Gela + bismuth sulfide nanorods), and PGTBi (PVA + Gela + Tau + bismuth sulfide nanorods). The scanning electron microscopy (SEM) images and size distribution histograms of non-crosslinked and thermally crosslinked nanofibers are shown in Fig. 2a, b and Fig. S2. The SEM images showed that both the non-crosslinked and thermally crosslinked nanofibrous scaffolds have a uniform, bead-less, continuous, and smooth morphology, indicating that thermal crosslinking did not change the morphology of the nanofibers. The diameters of all thermally crosslinked nanofibers were below 500 nm, closely resembling the fibrous architecture of native ECM collagen, which typically ranges from 50 to 500 nm in diameter.[45,46] The incorporation of Tau into nanofibers led to an increase in the average diameter of the thermally crosslinked nanofibers. This is attributed to the rise in solution viscosity upon the addition of Tau to the PG polymer solution.[32] As shown in the SEM micrographs and size distribution histograms in Fig. S2, the average diameter of thermally crosslinked nanofibers of PGBi is smaller than that of the average diameter of thermally crosslinked nanofibers of PG. The incorporation of Bi_2S_3 NRs into the electrospinning solution increases the solution conductivity and a greater charge density on the surface of the ejected jet during electrospinning, which leads to the imposition of a greater elongation force under the electric field, resulting in the reduced diameter of the nanofibers.[28,47] The obtained nanofiber scaffolds showed ideal morphological properties for skin tissue regeneration at the wound site.

The intermolecular interactions and functional groups in the nanofibers were analyzed using Fourier transform infrared (FTIR) as shown in Fig. 2c. The FTIR spectrum of PVA showed a band at about 3300–3500 cm^{-1} assigned to the stretching vibration of the O–H bond, and a band at 2940 cm^{-1} related to the C–H bond stretching vibration, and the bands at 1577 and 1433 cm^{-1} correspond to the stretching vibration of the C–O bond.[8,48,49] In the spectrum of Gela, the absorption band in the range of 3100–3500 cm^{-1} is related to the N–H stretching vibration of amide II and free O–H stretching vibration and the bands at 2960 and 2979 cm^{-1} were attributed to the C–H stretching vibration.[50,51] Furthermore, the strong absorption band at 1578 cm^{-1} was assigned to the C═O stretching vibration and hydrogen bonding coupled with COO^- stretching.[52] In the spectrum of the PG nanofiber scaffold, new bands were observed at 1652 cm^{-1} corresponding to the C═O stretching vibration of the ester and at 1093 and 1125 cm^{-1} due to the C–O stretching vibration of the ester.[52,53] Furthermore, the band observed in Gela at 1578 cm^{-1} corresponding to the COO^- group disappeared in the spectrum of the PG nanofiber, indicating the esterification reaction between the COOH groups of Gela and the OH groups of PVA.[52] The Tau spectrum showed characteristic bands attributed to the N–H stretching vibration of amine I and O–H stretching vibration at 2950 to 3200 cm^{-1}, N–H bending vibration of amine I at 1581 cm^{-1}, asymmetric stretching vibration of S═O at 1200 and 1213 cm^{-1}, symmetric stretching vibration of S═O at 1150 cm^{-1}, and stretching vibration of S–O at 736 cm^{-1}.[54–56] All characteristic bands of Tau were observed in PGT nanofibers, confirming the successful incorporation of Tau into the nanofibers. In the FTIR spectrum of Bi_2S_3 NRs, a band at 1116 cm^{-1} is present which is related to the Bi–S stretching vibration, indicating the successful synthesis of Bi_2S_3 NRs.[57] Furthermore, a band at 1579 cm^{-1} could be assigned to the C═O stretching vibration of the PVP polymer, which was shifted to a lower frequency by 77 cm^{-1} compared to the FTIR spectrum of PVP (1656 cm^{-1}). This change in the C═O band was due to the coordination interaction between the carbonyl group (C═O) of PVP and bismuth metal cations.[58] These results indicated that no new bonds were formed between Bi_2S_3 and PVP and the added PVP served as a good encapsulant. The spectrum of PGBi nanofibers was similar to the spectrum of PG nanofibers due to the low concentration of Bi_2S_3 NRs within the PGBi electrospinning solution. Therefore, the FTIR spectrum of the PGTBi nanofiber scaffolds was similar to the FTIR spectrum of the PGT nanofiber scaffolds, and similar bands were observed.

The X-ray diffraction (XRD) study was conducted to examine the crystalline structure of the raw material, Bi_2S_3 NRs, and nanofibers (Fig. 2d). The XRD pattern of PVA showed a peak at 19.84°, indicating its crystalline nature.[59] The broad peak at 19.79° in the XRD pattern for Gela confirmed its amorphous structure. The XRD spectrum of PG nanofibers showed a crystalline nature with a diffraction peak at 20°, which can be attributed to the crystalline structure of PVA and the formation of intra- and extra-molecular hydrogen bonds.[60] Tau exhibited a crystalline structure due to the presence of several characteristic diffraction peaks.[61,62] The diffraction pattern of Tau-loaded nanofibers (PGT and PGTBi) showed two new sharp peaks at 15.39° and 30.74° compared to PG nanofibers, confirming the presence of Tau and indicating its crystalline nature. The diffraction peaks of Bi_2S_3 NRs confirmed their

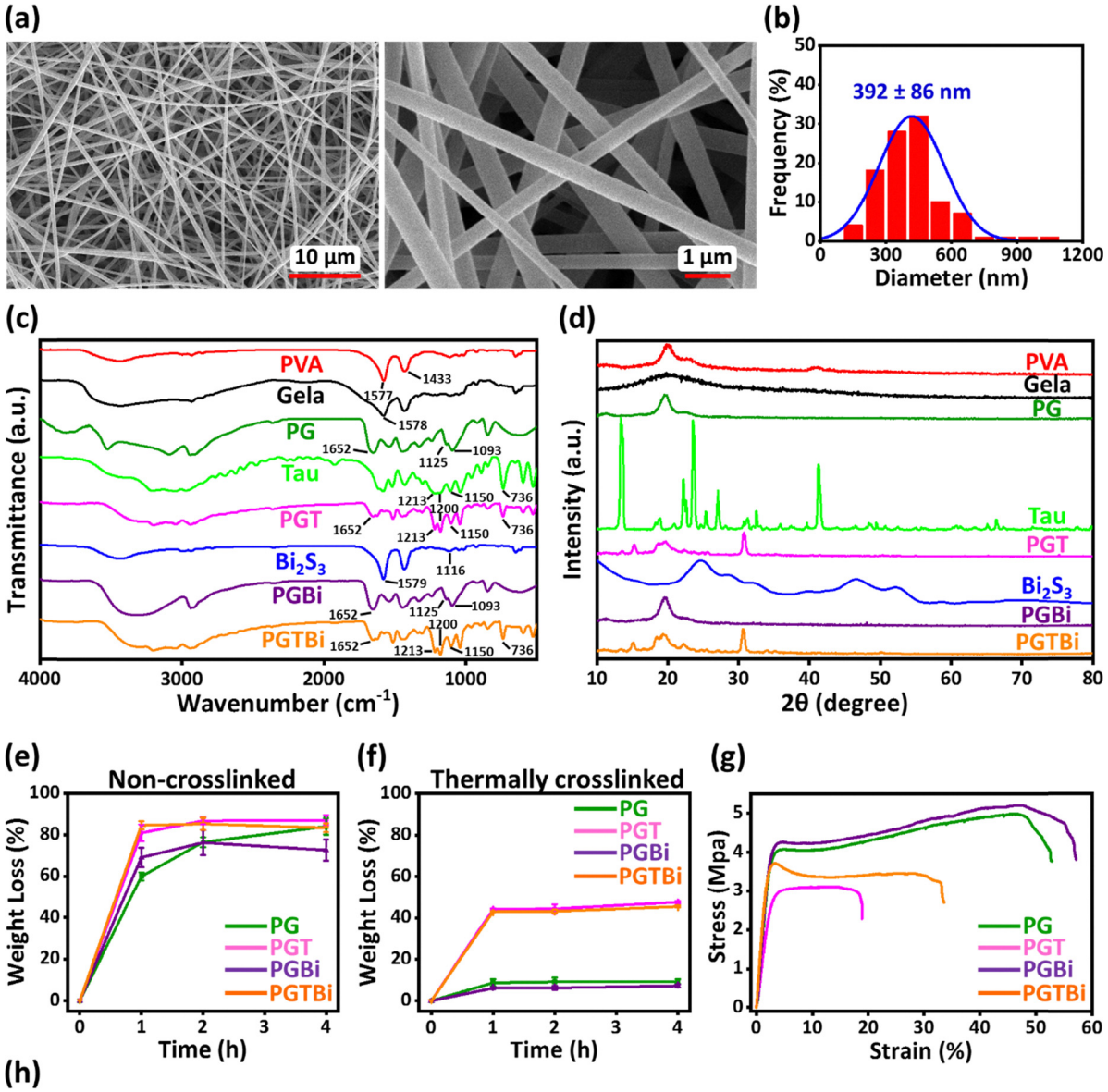

(h)

	PG	PGT	PGBi	PGTBi
Young's modulus (MPa)	128.7	102.7	154.8	150.8
Break strength (%)	47.4	18.5	47.8	33
Ultimate tensile strength (MPa)	4.9	2.9	5.2	3.2

Fig. 2 Physicochemical characterizations of nanofibrous scaffolds. (a) SEM micrographs of PGTBi nanofiber scaffolds. (b) Size distribution curve of PGTBi nanofiber scaffolds. (c) FTIR spectra of PVA, Gela, PG nanofiber, Tau, PGT nanofibers, Bi_2S_3 NRs, PGBi nanofibers, and PGTBi nanofibers. (d) XRD spectra of PVA, Gela, PG nanofibers, Tau, PGT nanofibers, Bi_2S_3 NRs, PGBi nanofibers, and PGTBi nanofibers. (e) *In vitro* degradation of non-crosslinking nanofiber scaffolds. (f) *In vitro* degradation of thermally crosslinking nanofiber scaffolds. (g) Stress–strain curves of nanofiber scaffolds. (h) Table of mechanical parameters of nanofiber scaffolds.

crystalline nature. However, the XRD spectrum of Bi_2S_3 NRs in PGBi nanofibers was not observed due to their small amount, and their XRD pattern is similar to that of PG nanofibers. The XRD pattern of PGTBi nanofibers was also similar to that of PGT nanofibers due to the low amount of Bi_2S_3 NRs. XRD data confirmed that Tau was successfully loaded into fibers while maintaining its crystalline nature during the electrospinning process.

Degradability is an important parameter in the application of nanofibrous patches for tissue regeneration.[63,64] The *in vitro*

degradation of the thermally crosslinked and non-crosslinked nanofibers was determined by measuring their weight loss in phosphate-buffered saline (PBS) solution. As shown in Fig. 2e, after 4 h incubation, all the non-crosslinked nanofibrous patches showed obvious weight loss of about 84% (PG), 87% (PGT), 72% (PGBi), and 83% (PGTBi), respectively. At the same time, the thermally crosslinked nanofibrous scaffolds displayed moderate weight loss of about 9% (PG), 47% (PGT), 7% (PGBi), and 45% (PGTBi), respectively (Fig. 2f). Thermally cross-linked samples of PGT and PGTBi illustrated a higher percentage of weight loss compared to thermally crosslinked PG and PGBi, which may be attributed to the presence of Tau and its influence on the hydrophilicity and dissolution behavior of the scaffolds or possibly the rapid release of Tau. These results indicate that thermal crosslinking is an effective method to improve the structural stability of nanofibrous scaffolds in culture media and biological fluids.

Fig. 2g displays the stress–strain curves of PG, PGT, PGBi, and PGTBi nanofiber scaffolds, and Fig. 2h shows Young's modulus, break strength, and ultimate tensile strength of nanofiber patches. As shown in Fig. 2g, with the addition of Tau into PG nanofibers, the tensile strength decreased, which is due to the increase in the viscosity of the solution and the subsequent increase in the diameter of nanofibers, which reduced the mechanical properties of PGT nanofiber scaffolds. The incorporation of Bi_2S_3 NRs into the PGBi nanofibrous patch could statistically improve their tensile strength. By adding Bi_2S_3 NRs to the PGBi electrospinning solution, solution viscosity and nanofiber diameter decreased, and as a result, the mechanical properties of PGBi nanofibers increased.[65] In addition, the properties of Bi_2S_3 NRs, such as high surface-to-volume ratio, strength, and rigidity, increased the tensile strength of PGBi nanofibers.[66] Here, the integration of natural and synthetic polymers provides sufficient mechanical properties against mechanical forces for skin tissue engineering.[67] Several studies demonstrate that the range of Young's modulus for skin tissue is between 15 and 150 MPa.[8,68,69] As shown in Fig. 2h, the value of Young's modulus for PGTBi nanofibers is 150.8 MPa, which is very close to the acceptable range of Young's modulus required for skin tissue.

Wettability is a key property of electrospun patches used in skin tissue engineering, as it influences the absorption of wound exudates, helps maintain a moist environment, and enhances cell adhesion, proliferation, and protein absorption.[70,71] The wettability of PG, PGT, PGBi, and PGTBi nanofibrous scaffolds was investigated by measuring the water contact angle. As illustrated in Fig. S3, water droplets placed on the nanofibrous scaffolds were rapidly absorbed into the porous fibrous network, resulting in immediate spreading and apparent contact angles approaching zero degrees. This behavior reflects the highly hydrophilic nature of the materials combined with capillary-driven liquid uptake within the interconnected nanofiber structure, rather than a conventional static contact angle measurement. Such rapid wetting behavior is commonly observed in highly porous electrospun scaffolds, where liquid penetration into the fibrous network occurs faster than the formation of a stable droplet interface. Nevertheless, it also shows the hydrophilic nature of the nanofibrous scaffolds. Studies have shown that Tau increases the wettability and water absorption capacity of nanofibrous scaffolds due to its hydrophilic nature.[32,72] In addition, PVA and Gela polymers have a hydrophilic nature due to the presence of hydrophilic functional groups in their chemical structure.[73] As a result, these nanofibers become highly hydrophilic, enabling them to provide a moist environment for wound healing.

The results and discussions of other physicochemical characterization of nanofibrous scaffolds, including the EDX (Fig. S4), and thermogravimetric and derivative thermogravimetry analysis (TGA and DTG; Fig. S5) are present in the supplementary information, indicating successful fabrication of the nanofibrous scaffolds.

2.4. Characterization of MNs with electrospun backing

SEM images of PH, PHA, PGTBi-PH, and PGTBi-PHA MN patches show a 10 × 10 array with a height of about 800 μm and a base width of about 200 μm (Fig. 3a). The chemical structure of PHA needles was examined by FTIR spectroscopy (Fig. 3b). The pure PMVE-MA spectrum showed characteristic bands at 1860, 1781, and 926 cm^{-1}, attributed to the C═O and C–O–C stretching vibration of the anhydride groups, respectively. In addition, the bands at 1225 and 1096 cm^{-1} were attributed to the vibration of the ether group (–OCH_3).[74,75] The FTIR spectrum of HA showed a broad stretching band at 3416 cm^{-1} assigned to O–H and N–H stretching vibrations.[76,77] Moreover, the sharp bands at 1620 and 1578 cm^{-1} were attributed to the carbonyl (C═O) stretching vibration of carboxylic acid and amide, respectively. Also, the absorption bands at 1150 and 1043 cm^{-1} correspond to the linkage stretching of C–OH and C–O–C in the HA structure, respectively.[78,79] In the spectrum of Alla, the bands observed at 3441 and 3346 cm^{-1} were related to symmetric vibrations of –NH_2 and –NH groups, and the absorption bands at 1780, 1716, and 1660 cm^{-1} were attributed to the stretching vibration of carbonyl groups in the imidazole ring and amide in the ureido group.[80,81] FTIR spectra of PH and PHA MN needles showed all the characteristic bands of PMVE-MA, HA, and Alla. In the PH and PHA spectrum, new bands were observed at 1717 and 1179 cm^{-1} corresponding to the C═O and C–O stretching vibration of ester, respectively, indicating the esterification reaction between the acid groups of PMVE-MA with the hydroxyl groups of HA. Furthermore, the bands observed in the PMVE-MA spectrum at 1860, 1781, and 926 cm^{-1}, attributed to the C═O and C–O–C stretching vibration of the anhydride groups, disappeared in the PH and PHA spectrum, indicating the successful ring-opening of PMVE-MA. The C–H stretching vibration of Alla at 3060 cm^{-1} was shifted to the lower wavenumbers (2997 cm^{-1}) in the FTIR spectrum of PHA MN needles, confirming the incorporation of the Alla into PH MN needles.

The XRD patterns of PMVE-MA, HA, Alla, and needles of PH and PHA are shown in Fig. 3c. Evaluation of the XRD spectrum of PMVE-MA and HA confirmed their amorphous nature. The XRD pattern of PH needles has an amorphous structure. The XRD pattern of Alla demonstrated many sharp peaks, indicating its

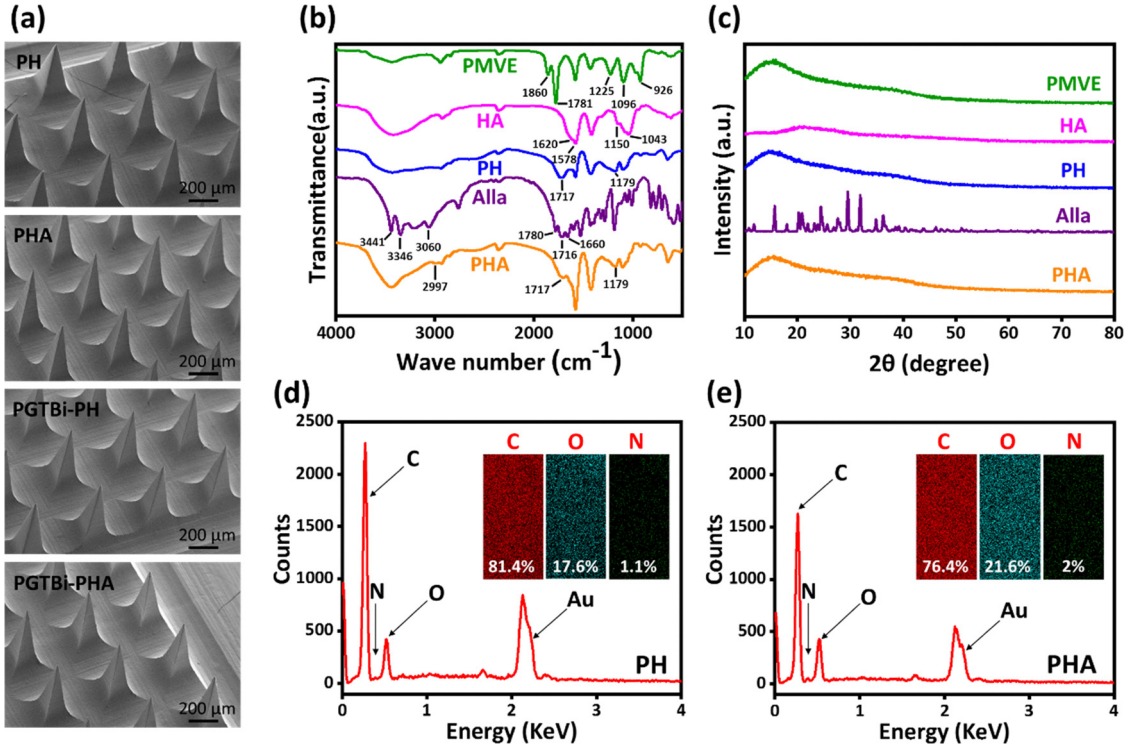

Fig. 3 Characterization of PGTBi-PHA MN patches. (a) SEM images of PH, PHA, PGTBi-PH, and PGTBi-PHA MN patches. (b) FTIR spectra of PMVE-MA, HA, PH MNs, Alla, and PHA MNs. (c) XRD patterns of PMVE-MA, HA, PH MNs, Alla, and PHA MNs. (d) EDX analysis of PH MNs. (e) EDX analysis of PHA MNs.

crystalline nature.[82] However, the Alla diffraction peaks were not observed in PHA needles, because the amount of Alla in the needles was low. Therefore, the XRD pattern of PHA needles is similar to that of PH and has an amorphous structure.

EDX elemental analysis showed the composition of PH and PHA needles (Fig. 3d and e). As expected, the weight percentages of O and N increased from 17.6% and 1.1% to 21.6 and 2%, respectively, indicating the incorporation of Alla into MNs.

2.5. Mechanical and insertion characterization of MN patches

Ensuring sufficient mechanical strength is a critical design requirement for MN patches to effectively penetrate the stratum corneum and facilitate drug delivery into the underlying skin layers. In our study, the PH, PHA, PGTBi-PH, and PGTBi-PHA MN patches demonstrated robust mechanical properties, as evidenced by mechanical compression testing and successful insertion into both Parafilm M® layers and rat cadaver skin. These results highlight the structural integrity and functional reliability of the patches under physiologically relevant conditions. We used pyramidal geometry as it can enhance mechanical strength compared to conical shape MNs, likely due to its broader cross-sectional area at the base, which improves load distribution and resistance to deformation. This design advantage not only ensures consistent skin penetration but also enhances the clinical applicability of the patches by reducing the risk of mechanical failure during administration.[83] As shown in Fig. 4a, the maximum failure force for the PH, PHA, PGTBi-PH, and PGTBi-PHA MN patches was 0.44, 0.59, 0.51, and 0.57 N per needle, respectively, which was statistically significantly more than the force required to penetrate human skin (~0.1 N).[84,85] The results also showed that PHA and PGTBi-PHA MN patches needed more force to create the same displacement, indicating that the Alla drug has increased the mechanical strength of the MN patches. Furthermore, the fracture force of MN patches with and without the electrospun nanofiber backing layer was almost similar, indicating that the electrospun nanofiber backing layer did not affect the mechanical strength of the needles in the PGTBi-PH and PGTBi-PHA MN patches.

The insertion capability of the PH, PHA, PGTBi-PH, and PGTBi-PHA MN patches was evaluated using an eight-layer Parafilm M® model, a widely accepted skin simulant.[86,87] The images and graph in Fig. 4b and c show the MN inserted Parafilm M® layers as well as holes created as a function of depth, respectively. The results showed that the MN patches completely pierced the first and second Parafilm M® layers and reached the fourth layer. Given that the average thickness of each Parafilm M® layer is about 127 μm,[88] the penetration depth is approximately 508 μm, equivalent to 70% of the height of the loaded MN patches with and without Alla. This observation indicates that the MN patches are capable of penetrating into skin layers, suggesting the potential for intratissue exposure of the loaded Alla following microneedle dissolution.

To further evaluate skin penetration ability, the MN patches were applied to the rat cadaver skin and detached after 1 min. As shown in Fig. 4d, for all MN patches, a 10 × 10 array of the blue microchannels was visible on the skin surface, indicating

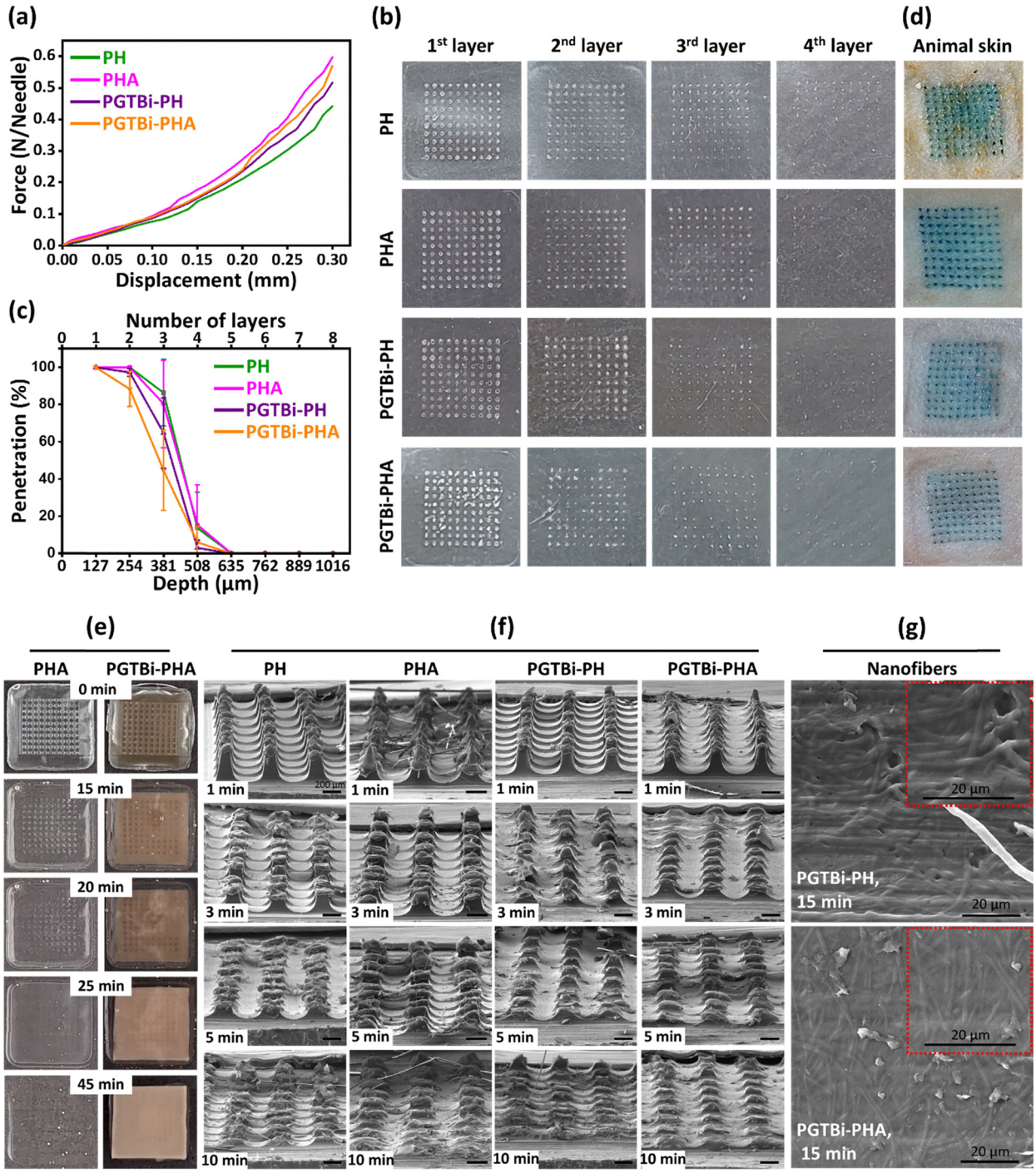

Fig. 4 Mechanical and dissolution characterization of PH, PHA, PGTBi-PH, and PGTBi-PHA MN patches. (a) Force *vs.* displacement curves of MN patches. (b) Images of the first, second, third, and fourth layers of Parafilm M® after insertion of MN patches with an applicator. (c) Linear curves representative of the percentage of holes created by MN patches as a function of depth. Data are presented as mean ± SD (N = 3). (d) Images of rat cadaver skin after the insertion of MNs loaded with trypan blue. (e) Images of *in vitro* dissolution of PHA and PGTBi-PHA MN patches in PBS for 0, 15, 20, 25, and 45 min. (f) SEM images of *in vivo* dissolution of PH, PHA, PGTBi-PH, and PGTBi-PHA MN patches after insertion into the wound bed created on rat skin. (g) SEM image of electrospun fibers 15 min after the insertion of the MN patches into the wound bed, resulting in the dissolution of the needles and exposure of the fibers to the wound bed.

that 100% of the needles had sufficient mechanical strength to penetrate the cuticle layer of the skin. These results demonstrated that MN patches with and without the electrospun nanofiber backing layer had sufficient mechanical strength to penetrate skin. Overall, the combination of strong mechanical performance and effective insertion capability underscores the potential of PGTBi-PHA MN patches as a reliable platform for drug delivery to the deep areas of the skin wound.

2.6. *In vitro* and *in vivo* dissolution of MN patches

Dissolution of MNs is an important factor in drug release.[89] Therefore, the dissolution behavior of PH, PHA, PGTBi-PH, and PGTBi-PHA MN patches was evaluated. *In vitro* dissolution of PHA and PGTBi-PHA MN patches was performed in PBS solution (pH 7.4). As shown in Fig. 4e, the needles were dissolved completely in 15 min. After 45 min, just the electrospun part of the backing layer remained while the surrounding polymers were also dissolved. This observation confirms that the needle arrays, together with the non-electrospun segment of the backing layer, can fully dissolve within the wound bed through gentle hydration from the wound's natural exudate and fluids. This dissolution process strategically exposes the underlying nanofibers of the backing layer directly to the wound site, creating an ideal scaffold that promotes robust cell attachment, migration, and proliferation to accelerate the healing process.

The dissolution study of the MNs in the wound bed (Fig. 4f) clearly indicates that about half the height of the needles in all types of MN patches dissolved within the first minute following insertion into the wound. The dissolution reached approximately 70% of the needle height within 3 minutes (Fig. 4f), with the needles fully disappearing after 5 minutes. This fast dissolution behavior of MN patches is due to the highly water-soluble properties of PMVE-MA and HA polymers.[90] In addition, the progressive dissolution of both the microneedles and the non-electrospun segment of the backing layer exposes the underlying electrospun nanofiber layer (Fig. 4g) to the wound bed, which remains as a dressing to facilitate long-term cell attachment, migration, and healing. This architecture enables initial microneedle penetration and rapid needle dissolution while leaving the electrospun layer in contact with the wound surface, where it can act as a potential reservoir for the loaded therapeutic component. Also, this approach can minimize potential discomfort from prolonged needle presence and supports faster healing processes.

2.7. Biocompatibility of the MN patches

2.7.1. Hemocompatibility of the MN patches. Hemocompatibility is one of the essential prerequisites for biomaterials used in novel wound dressings.[91] The blood compatibility of PG, PGT, PGBi, and the PGTBi nanofiber scaffolds was evaluated after 1, 4, 8, and 24 h incubation with human erythrocytes with different weights of 1, 2, 4, and 8 mg at room temperature. According to the National Biological Safety Protocol, if erythrocyte lysis is less than 5%, it indicates good compatibility with the material.[92,93] As shown in Fig. 5a–d, the percentages of non-hemolyzed red blood cells in all nanofiber scaffolds at different weights were higher than 95%. In addition, as shown in Fig. 5e, red blood cells treated with PGTBi nanofibrous scaffolds (weights of 2 and 8 mg) were precipitated after centrifugation, and all samples had a transparent supernatant similar to the negative control group (PBS; pH 7.4).

Furthermore, the blood compatibility of PH and PHA needles of MN patches was evaluated at concentrations of 50, 100, 200, and 400 μg ml^{-1} after 1, 4, 8, 24 and 48 h incubation by hemolysis assay. The results showed that the percentage of non-hemolyzed red blood cells in PH and PHA needles is above 99% in all concentrations (Fig. 5f and g). Also, as shown in Fig. 5h, the supernatant at concentrations of 100 and 400 μg ml^{-1} PH and PHA needles is completely transparent and similar to the negative control group (PBS; pH 7.4). These results indicated that the novel PGTBi-PHA MN patches have good blood compatibility and are safe for wound healing.

2.7.2. *In vitro* cytocompatibility of MN patches. Electrospun nanofibers should have good biocompatibility to create a suitable microenvironment for cell growth and proliferation during tissue repair.[94] Here, we investigated the safety of PG, PGT, PGBi, and PGTBi nanofibrous scaffolds using the live/dead assay on L929 mouse fibroblast cells. The viability, proliferation, and adhesion of L929 cells seeded onto the nanofibrous scaffolds are shown in Fig. 6a after 4 and 11 days of incubation. All four samples showed excellent cell adhesion and viability. In addition, a gradual increase in the population of viable cells (green fluorescence points) was observed among all groups from day 4 to 11. Also, the morphology of the cells changed from partially spherical to more spindle-shaped over time, which indicates the adhesion of the cells to the surface of the nanofibers and their expansion.[95] These results indicated that PG, PGT, PGBi, and PGTBi nanofibrous scaffolds are safe and non-cytotoxic, and can provide a suitable environment for cell adhesion and proliferation.

Furthermore, the cytotoxicity of PH and PHA MN needles on the L929 cell line was evaluated using the CellTiter-Glo assay after 24 and 48 h of incubation. As shown in Fig. 6b, more than 90% cell viability was observed for PH and PHA MN needles at different concentrations and time points. These findings indicate that PGTBi-PHA MN patches are safe, non-toxic, and suitable for wound healing and tissue regeneration.

2.8. Antibacterial activity of the PGTBi nanofibers

The growth of bacteria on the wound bed leads to inflammation and infection and delays the healing process. Therefore, the antibacterial property of regenerative formulations is a vital factor in skin wound healing.[96,97] Studies have shown that bacteria could be destroyed at temperatures above 50 °C by inactivating some enzymes and proteins.[98,99] Therefore, the photothermal antibacterial capability of the electrospinning patch was investigated by the colony counting method against Gram-negative *Escherichia coli* (*E. coli*) and Gram-positive *Staphylococcus aureus* (*S. aureus*) with and without 808 nm light irradiation. As shown in Fig. 6c, after 10 min of exposure to 808 nm laser light, only a few *E. coli* and *S. aureus* colonies were observed in the PGTBi group on the agar plate. In contrast, without laser irradiation, there was statistically significant bacterial growth on the surface of agar. In contrast, several bacterial colonies were visible in the control group (normal saline) with and without laser light irradiation. These results show that PGTBi nanofibers have a good antibacterial effect against *E. coli* and *S. aureus* due to the heat generation by the laser light radiation on the Bi_2S_3 NRs loaded in the PGTBi nanofibers. Bi_2S_3 NRs are an n-type semiconductor with good biocompatibility, high absorption coefficient, and narrow band gap, which exhibit

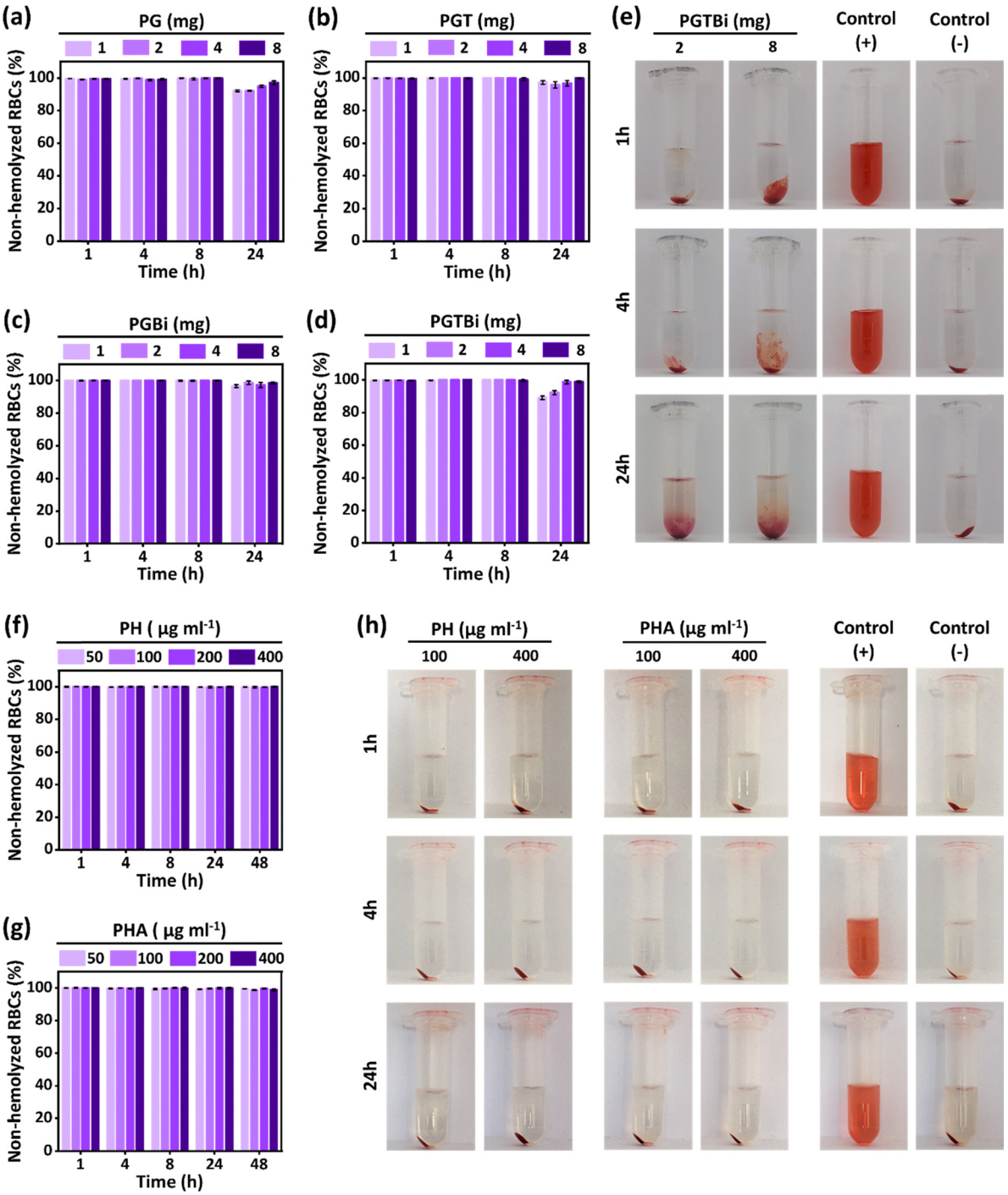

Fig. 5 Hemolytic activity of (a) PG, (b) PGT, (c) PGBi, and (d) PGTBi nanofibrous scaffolds after 1, 4, 8, and 24 h incubation with human RBCs with different weights of 1, 2, 4, and 8 mg at room temperature. (e) Photographs of 2 and 8 mg PGTBi nanofibrous scaffolds and positive and negative control groups after 1, 4, and 24 h incubation with human RBCs. (f and g) Hemolytic activity of PH and PHA needles after 1, 4, 8, 24 and 48 h incubation with human RBCs with different concentrations of 50, 100, 200, and 400 μg ml^{-1} at room temperature. (h) Photographs of 100 and 400 μg ml^{-1} PH and PHA needles and positive and negative control groups after 1, 4, and 24 h incubation with human RBCs. Data are presented as mean ± SD (N = 3).

excellent antibacterial properties under NIR light irradiation due to high photothermal conversion efficiency.[100,101]

2.9. *In vivo* toxicity of MN patches

The biosafety of the MN patches was evaluated by H&E staining of the main organs of rats (kidneys, spleen, and liver) and monitoring the blood biochemical and hematological parameters. As shown in Fig. 7a, there were no statistically significant differences in hematological factors compared to the control group, including the blood levels of RBCs, hemoglobin (HGB), hematocrit (HCT), platelets (PLT), white blood cells (WBCs), neutrophils (NEUT), lymphocytes (LYMPH), and monocytes (MONO). Furthermore, no obvious

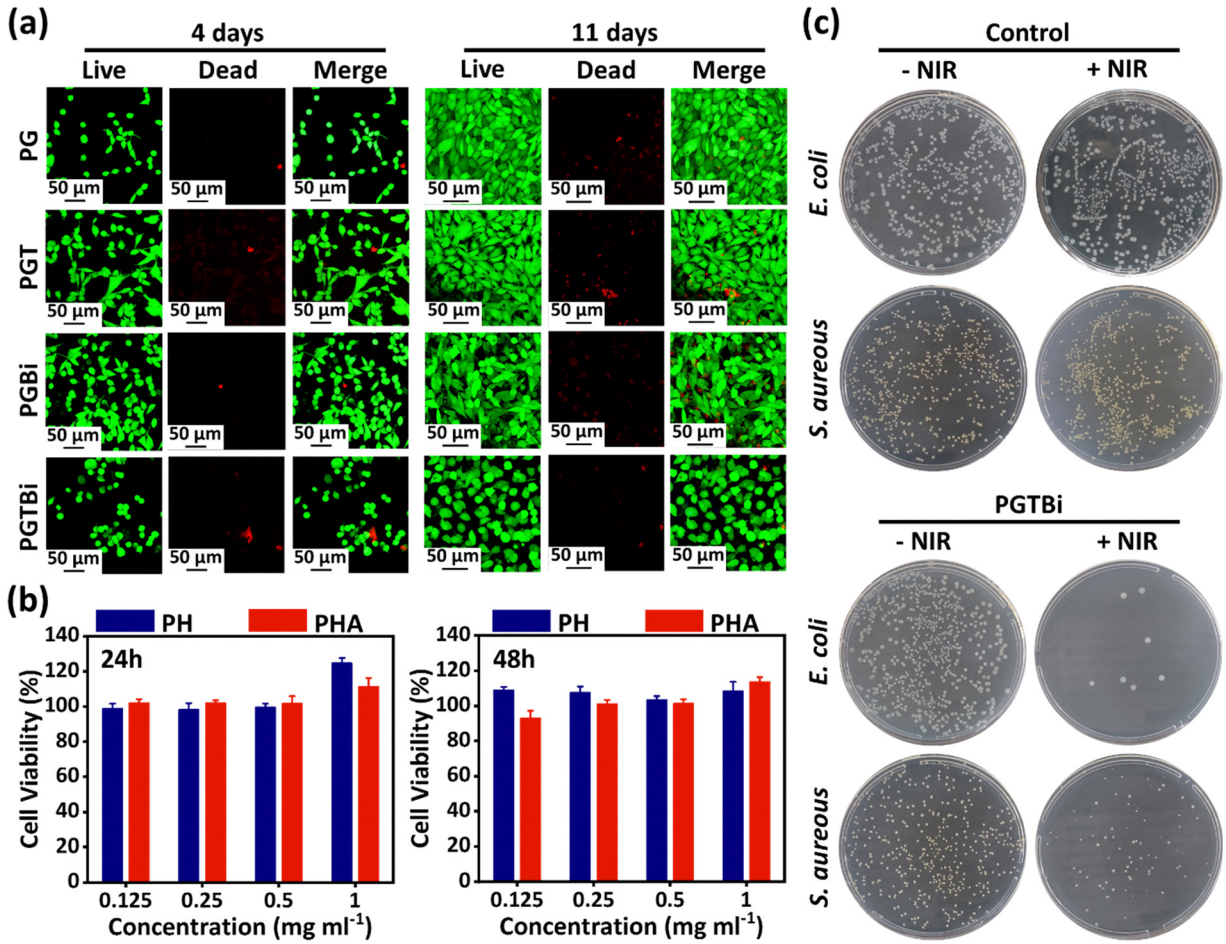

Fig. 6 (a) Representative images of live/dead staining of L929 cells cultured on the surface of PG, PGT, PGBi, and PGTBi nanofibrous scaffolds after 4 and 11 days (green: live cells and red: dead cells). (b) Cell viability of L929 fibroblast cells treated with 0.125, 0.25, 0.5, and 1 mg ml^{-1} of PH and PHA MN needles for 24 and 48 h at 37 °C, quantified by the CellTiter–Glo luminescence assay. Data are presented as mean ± SD (N = 4). (c) Photographs of the *in vitro* antibacterial activity of PGTBi nanofibrous scaffolds.

toxicity of MN patches was observed in biochemical indexes and minerals, such as total protein (TP), albumin (ALB), calcium (Ca), phosphor (Ph), blood urea nitrogen (BUN), creatinine (Cr), and alkaline phosphatase (ALP). Just lactate dehydrogenase (LDH) in some MN-treated groups appear higher than those of the control group. LDH is a nonspecific enzyme that can be transiently elevated due to localized tissue remodeling, skin injury, inflammation, or active wound healing rather than systemic toxicity. In the present study, MN insertion itself and the accelerated tissue regeneration process are expected to induce temporary cellular turnover and metabolic activity at the wound site, which can be the contributing factor to increases in circulating LDH levels. Nevertheless, no toxic pathological changes such as tissue necrosis or inflammatory cell infiltration were observed in the major organs (kidneys, spleen, and liver) in the groups inserted with MN patches (Fig. 7b). These results indicated that MN patches are safe for wound healing and biomedical applications.

2.10. *In vivo* wound healing assessment

The healing process of the infected wounds was monitored by photography on days 0, 3, 7, 10, and 14.[102] As shown in Fig. 8a and c, the wound area of the PGTBi-PHA + NIR-treated group was significantly reduced compared to the control group after 7 days of treatment. The wound closure rate on day 10 was 17.3% for the PGTBi-PHA + NIR-treated group. In contrast, the data for the control, PGT-PHA, and PGTBi-PHA-treated groups were 33.9%, 29.8% and 27.5%, respectively, confirming the PTT effect to promote wound healing (Fig. 8b). Furthermore, on day 14, the wound almost healed completely (96.1%) for the PGTBi-PHA + NIR-treated group, but 19.5, 8.4, and 7.3% of wounds in the control, PGT-PHA, and PGTBi-PHA-treated groups remained open with uneven scars, respectively.

To further evaluate the wound healing efficacy of MN patches, histological analysis of the wound tissue was performed by H&E and Masson's trichrome staining on day 14 of screening. As shown in Fig. 8d, in the control group, a thick epidermis was observed along with a large number of inflammatory cells with the minimum thickness of granulation tissue, indicating a delay in the wound healing process. In contrast, the PGTBi-PHA + NIR-treated group showed more regular epidermis structure, maximum granulation tissue thickness, and the formation of hair follicles and sebaceous glands,

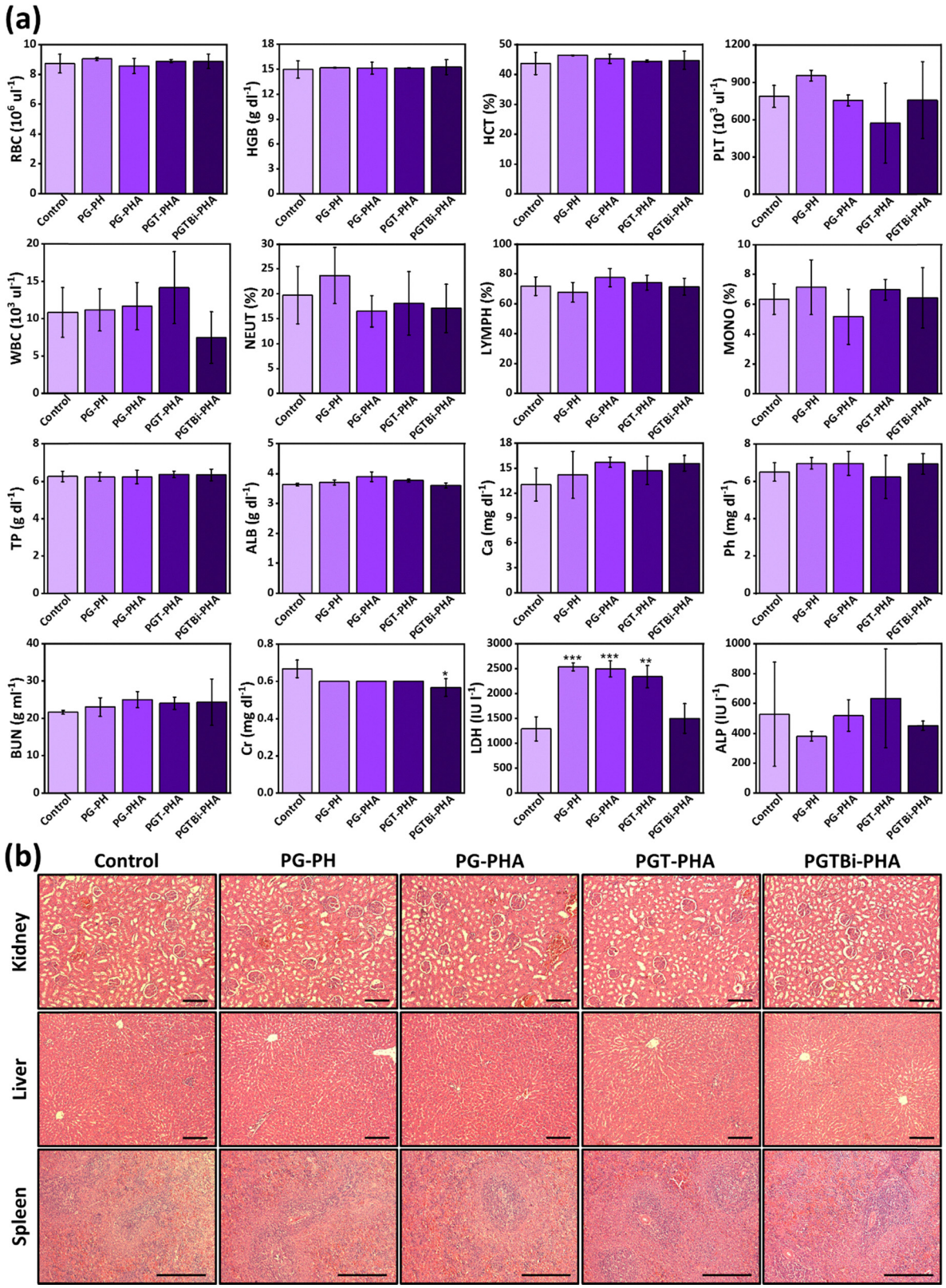

Fig. 7 *In vivo* toxicity evaluation of PG-PH, PG-PHA, PGT-PHA, and PGTBi-PHA MN patches. (a) Hematological factors of animals for groups with MN patches inserted. Data are presented as mean ± SD (N = 3), the statistical analysis was performed using one-way ANOVA (*$p < 0.05$, **$p < 0.01$, ***$p < 0.001$ *vs.* control group). (b) H&E staining of liver, kidney, and spleen organs of rats 14 days after insertion of the MN patches (scale bar = 200 μm).

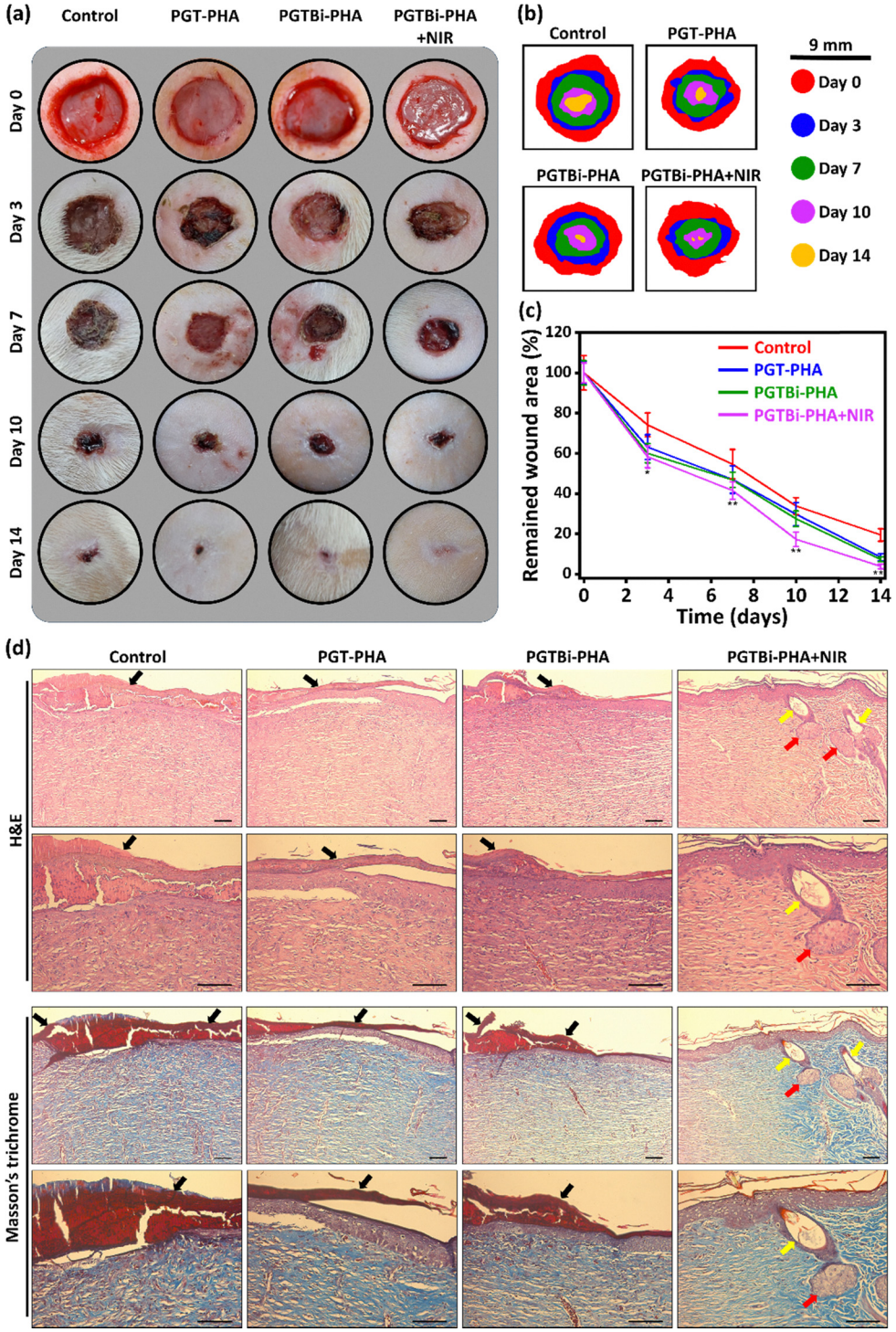

Fig. 8 *In vivo* wound healing assessment. (a) Photographs of the skin wounds of control, PGT-PHA, PGTBi-PHA and PGTBi-PHA + NIR-treated groups on days 0, 3, 7, 10, and 14 (scale bar = 20 mm). (b) Schematic representation of morphological changes of the wound healing process at different time points. (c) Quantitative analysis of the remaining wound area (%) for different treatment groups at days 0, 3, 7, 10, and 14. Data are presented as mean ± SD ($N = 6$). Statistical analysis was performed using one-way ANOVA, and statistically significant differences between PGTBi-PHA + NIR (purple line) and the control (red line) group are indicated (*$p < 0.05$, **$p < 0.01$). (d) Images of H&E and Masson's trichrome staining of histological sections in different groups after 14 days. Scabs, hair follicles, and sebaceous glands are shown with black, yellow, and red arrows, respectively (scale bar = 200 μm).

indicating better tissue regeneration. Moreover, the PGTBi-PHA-treated group did not show any scab, while it was observed in the control and other treated groups. Also, fewer inflammatory cells, higher density of fibroblasts, and more new blood vessels were observed in the MN patch-treated groups compared to the control group, which is due to the

synergistic anti-inflammatory and cell proliferation effect of Alla and Tau. In a study performed by V. Nosrati-Siahmazgi *et al.*, H&E-stained tissue in the Alla-treated group showed increased fibroblast proliferation, migration, and fewer inflammatory cells in the wound area compared to the other groups.[103] Furthermore, mild NIR light irradiation in the PGTBi-PHA + NIR-treated group induced proliferation, differentiation, and angiogenesis of endothelial cells, as well as enhanced antibacterial function, leading to excellent efficacy in wound healing.[104] According to Masson's trichrome staining, the MN patch-treated groups showed denser collagen deposition with a more regular fibrous structure than the control group, indicating rapid wound healing with ECM remodeling and tissue regeneration through combined therapy. Quantitative analysis of tissues stained with H&E and Masson trichrome was performed to demonstrate fibroblast cell density, granulation tissue thickness, inflammatory cell density, and collagen deposition (Fig. S7). As shown in Fig. S7a, b, and d, the density of fibroblast cells, the thickness of granulation tissue, and collagen deposition in the MN patch-treated groups were significantly higher than those in the control group. On the other hand, the density of inflammatory cells was significantly reduced in the MN patch-treated groups (Fig. S7c).

These results indicated that the PGTBi-PHA + NIR MN patch accelerated wound healing and skin regeneration, which is due to combined elevated local temperature, antibacterial activity of the formulation, and combinatory effect of formulation components that induces anti-inflammatory, angiogenesis, cell proliferation, and ECM formation responses. It is noteworthy to highlight that while the integrated PGTBi-PHA patch demonstrated enhanced wound-healing outcomes compared with control and partial systems, the present study does not aim to quantitatively isolate the individual contributions of each component or to establish strict pharmacological synergy. Instead, the results support the feasibility and therapeutic potential of a sequential delivery strategy combining rapid MN-mediated delivery with the electrospun nanofiber layer as a reservoir for surface-level availability of Tau due to its scaffold structure and gradual degradation behavior.

2.11. Considerations for translation and manufacturing

From a translational perspective, the integration of electrospun nanofibers, inorganic photothermal nanorods, dual bioactive agents, and dissolvable microneedles introduces manufacturing complexity that warrants consideration. In the present study, process reproducibility was supported by controlled fabrication parameters, including polymer concentration, electrospinning voltage and flow rate, and mold-based microneedle casting. Fiber diameter distribution was consistently monitored by SEM analysis, Bi_2S_3 nanorod incorporation was verified by EDX, and microneedle geometry was confirmed by SEM imaging and mechanical testing. These characterization studies provide initial evidence of structural consistency across batches at the laboratory scale.

For scale-up, electrospinning and microneedle molding are both established and industrially scalable technologies. Process control strategies such as in-line monitoring of fiber diameter, nanoparticle dispersion homogeneity, and microneedle dimensional accuracy would be required for large-scale production. Quantitative quality control metrics (*e.g.*, drug content uniformity, Bi content per patch, mechanical strength thresholds) would be necessary to ensure batch-to-batch reproducibility.

Regarding sterilization, potential methods include gamma irradiation and ethylene oxide treatment, both commonly used for polymeric medical devices. However, their effects on polymer integrity, drug stability, and nanorod photothermal performance would require systematic evaluation. For example, gamma irradiation may induce polymer chain scission, while ethylene oxide could affect residual solvent levels; therefore, post-sterilization mechanical, chemical, and photothermal assessments would be essential.

From a regulatory standpoint, Bi_2S_3 nanorods function as localized photothermal agents and are not intended for systemic exposure. Nevertheless, long-term biodistribution, clearance, and toxicological profiling would be required prior to clinical translation, particularly for repeated applications. Future studies will focus on comprehensive pharmacokinetic and immunological evaluation to support regulatory approval pathways.

Overall, while the present study establishes proof-of-concept feasibility and short-term safety, further manufacturing optimization, sterilization validation, and regulatory-focused investigations will be necessary for clinical translation.

3. Conclusions

In summary, an electrospun patch with photothermal properties was successfully incorporated into the backing layer of MNs for wound healing applications. The PGTBi-PHA MN patch was fabricated using a molding method and a two-step casting process. After applying the PGTBi-PHA MN patch to the wound bed, the PHA needles rapidly dissolved upon hydration, which may facilitate intratissue exposure of Alla. Meanwhile, the electrospun nanofiber scaffold remained at the wound interface, providing structural support and a potential reservoir for bioactive components. Then, the PGTBi nanofiber scaffolds were simultaneously exposed to NIR light, and the loaded Bi_2S_3 NRs rapidly converted the light energy into heat, killing the bacteria. In addition, PGTBi nanofiber scaffolds serve as a wound dressing on the wound bed. Due to the structural similarity of electrospun nanofibers, Gela, and HA with ECM, the MN patch can provide a suitable substrate for cell attachment, migration, proliferation, and differentiation. Loading Alla and Tau into the MN patch along with the photothermal effect of Bi_2S_3 NRs synergistically accelerated the wound healing process by reducing skin irritation and providing antioxidant, keratolytic, anti-inflammatory, and antibacterial activity. Overall, this study demonstrates the feasibility of a hybrid

dissolvable MN-electrospun fiber platform for sequential wound-healing support, combining rapid intratissue delivery with surface-level therapy. The findings provide a foundation for future optimization and mechanistic studies aimed at further improving therapeutic performance.

4. Experimental section

Experimental details are described in the SI.

Conflicts of interest

The authors declare no competing interests. The authors declare Patent applications or registrations.

Data availability

The data analysis of this article is available in the interactive notebook of Maryam Toolabi and can be provided upon request from the authors.

Supplementary information (SI) is available. See DOI: https://doi.org/10.1039/d5ma01289a.

Acknowledgements

M. T. acknowledges financial support from the School of Pharmacy, Zanjan University of Medical Sciences, Zanjan, Iran, under the framework of the thesis project (No. A-12-1296-10) with the ethical code of IR.ZUMS.REC.1400.439. Y. Z acknowledges financial support from the De Cock-Hadders Foundation. The authors acknowledge financial support from the UMCG Research Funds.

References

1 H. Chen, G. Lan, L. Ran, Y. Xiao, K. Yu, B. Lu, F. Dai, D. Wu and F. Lu, *Carbohydr. Polym.*, 2018, **183**, 70–80.
2 Y. Yang, Y. Liang, J. Chen, X. Duan and B. Guo, *Bioact. Mater.*, 2022, **8**, 341–354.
3 M. El-Aassar, O. M. Ibrahim, M. M. Fouda, N. G. El-Beheri and M. M. Agwa, *Carbohydr. Polym.*, 2020, **238**, 116175.
4 C. Gao, L. Zhang, J. Wang, M. Jin, Q. Tang, Z. Chen, Y. Cheng, R. Yang and G. Zhao, *J. Mater. Chem. B*, 2021, **9**, 3106–3130.
5 X. Liu, H. Xu, M. Zhang and D.-G. Yu, *Membranes*, 2021, **11**, 770.
6 O. E. Fayemi, A. C. Ekennia, L. Katata-Seru, A. P. Ebokaiwe, O. M. Ijomone, D. C. Onwudiwe and E. E. Ebenso, *ACS Omega*, 2018, **3**, 4791–4797.
7 K. Wu, X. Wu, J. Guo, Y. Jiao and C. Zhou, *Adv. Healthcare Mater.*, 2021, **10**, 2100793.
8 P. Sobhanian, M. Khorram, S.-S. Hashemi and A. Mohammadi, *Int. J. Biol. Macromol.*, 2019, **130**, 977–987.
9 H. Ejegu, M. Xu, C. Kumah, Y. Qingshuai, B. Fentahun, S. Yifan, B. Xin, G. Xu and H. Shen, *Int. J. Biol. Macromol.*, 2025, **309**, 142875.
10 S. Fahimirad, P. Satei, A. Latifi, S. Changizi-Ashtiyani, M. Bahrami and H. Abtahi, *J. Biomater. Sci., Polym. Ed.*, 2024, **35**, 2484–2505.
11 Y. Tan, Y. Wang, N. Zeng, Q. Zhang, M. Wu and Y. Wu, *Adv. Ther.*, 2024, **7**, 2300264.
12 X. Yang, W. Cao, X. Gu, L. Zheng, Q. Wang, Y. Li, F. Wei, T. Ma, L. Zhang and Q. Wang, *Int. J. Pharm.*, 2023, **647**, 123543.
13 Y. C. Pan, S. H. Wu, H. P. Tsai, M. H. Tai, C. J. Lin, H. W. Yang and S. H. Huang, *Adv. NanoBiomed Res.*, 2025, **5**, 2500010.
14 Y. Xie, Z. Wu, J. Wang, Z. Li and Z. Hu, *ACS Appl. Mater. Interfaces*, 2025, **17**, 25152–25162.
15 Y. Yin, H. Zhou, K. Liu, A. Wu and H. Zang, *Int. J. Biol. Macromol.*, 2025, 149835.
16 S. Mehmood, I. Ullah, Z. Hussain, H. Dawit, S. Ullah, X. Liu, W. Ahmed, M. Xu, Y. Cao and R. Pei, *Adv. Funct. Mater.*, 2025, e04317.
17 L. Yang, Y. Gao, Q. Liu, W. Li, Z. Li, D. Zhang, R. Xie, Y. Zheng, H. Chen and X. Zeng, *Small*, 2024, **20**, 2307104.
18 X. Zhang, G. Chen, L. Sun, F. Ye, X. Shen and Y. Zhao, *Chem. Eng. J.*, 2021, **406**, 126741.
19 T. Ma, X. Zhai, Y. Huang, M. Zhang, X. Zhao, Y. Du and C. Yan, *Adv. Healthcare Mater.*, 2021, **10**, 2100033.
20 J. Li, Y. Wang, J. Yang and W. Liu, *Chem. Eng. J.*, 2021, **420**, 127638.
21 Y. Chen, C. Zhang, X. Weng, S. Jiang and B. Cheng, *J. Photochem. Photobiol., B*, 2025, 113273.
22 M. Li, X. Liu, L. Tan, Z. Cui, X. Yang, Z. Li, Y. Zheng, K. W. K. Yeung, P. K. Chu and S. Wu, *Biomater. Sci.*, 2018, **6**, 2110–2121.
23 X. Xu, X. Liu, L. Tan, Z. Cui, X. Yang, S. Zhu, Z. Li, X. Yuan, Y. Zheng and K. W. K. Yeung, *Acta Biomater.*, 2018, **77**, 352–364.
24 S. Zhu, B. Zhao, M. Li, H. Wang, J. Zhu, Q. Li, H. Gao, Q. Feng and X. Cao, *Bioactive materials*, 2023, **26**, 306–320.
25 J. He, M. Shi, Y. Liang and B. Guo, *Chem. Eng. J.*, 2020, **394**, 124888.
26 X. Qi, W. Pan, X. Tong, T. Gao, Y. Xiang, S. You, R. Mao, J. Chi, R. Hu and W. Zhang, *Carbohydr. Polym.*, 2021, **264**, 118046.
27 Y. Wu, Y. Liang, Y. Liu, Y. Hao, N. Tao, J. Li, X. Sun, M. Zhou and Y.-N. Liu, *J. Mater. Chem. B*, 2021, **9**, 3224–3234.
28 W. Yang, Y. Li, L. Feng, Y. Hou, S. Wang, B. Yang, X. Hu, W. Zhang and S. Ramakrishna, *Int. J. Mol. Sci.*, 2020, **21**, 4224.
29 Y. Qi, S. Ren, J. Ye, Y. Tian, G. Wang, S. Zhang, L. Du, Y. Li, Y. Che and G. Ning, *Acta Biomater.*, 2022, **143**, 445–458.
30 Tarachand, V. G. Sathe and G. S. Okram, *AIP Conf. Proc.*, 2018, **1953**, 030190.
31 S. Dincer, A. Babül, D. Erdoğan, C. Özoğul and S. Dinçer, *Amino Acids*, 1996, **10**, 59–71.

32 S. Farzamfar, M. Naseri-Nosar, H. Samadian, S. Mahakizadeh, R. Tajerian, M. Rahmati, A. Vaez and M. Salehi, *J. Bioact. Compat. Polym.*, 2018, **33**, 282–294.
33 Z. Değim, N. Celebi, H. Sayan, A. Babül, D. Erdoğan and G. Take, *Amino Acids*, 2002, **22**, 187–198.
34 M. Haki, A. Shamloo, S.-S. Eslami, F. Mir-Mohammad-Sadeghi, S. Maleki and A. Hajizadeh, *Int. J. Biol. Macromol.*, 2023, **253**, 127051.
35 H. Zhu, H. T. Ao, Y. Fu, C. Zou, Z. Chen, Z. Jin, H. Zhou, B. Sun and S. Guo, *Int. J. Biol. Macromol.*, 2024, **275**, 133524.
36 X. Zhao, X. Li, P. Zhang, J. Du and Y. Wang, *J. Controlled Release*, 2018, **286**, 201–209.
37 J. Du, Z. Gu, L. Yan, Y. Yong, X. Yi, X. Zhang, J. Liu, R. Wu, C. Ge and C. Chen, *Adv. Mater.*, 2017, **29**, 1701268.
38 Y. Wang, Y. Wu, Y. Liu, J. Shen, L. Lv, L. Li, L. Yang, J. Zeng, Y. Wang and L. W. Zhang, *Adv. Funct. Mater.*, 2016, **26**, 5335–5344.
39 J. Liu, X. Zheng, L. Yan, L. Zhou, G. Tian, W. Yin, L. Wang, Y. Liu, Z. Hu and Z. Gu, *ACS Nano*, 2015, **9**, 696–707.
40 S. Huang, H. Liu, K. Liao, Q. Hu, R. Guo and K. Deng, *ACS Appl. Mater. Interfaces*, 2020, **12**, 28952–28964.
41 C. Chen, P. Zhou, C. Huang, R. Zeng, L. Yang, Z. Han, Y. Qu and C. Zhang, *Carbohydr. Polym.*, 2021, **273**, 118557.
42 P. Lei, R. An, P. Zhang, S. Yao, S. Song, L. Dong, X. Xu, K. Du, J. Feng and H. Zhang, *Adv. Funct. Mater.*, 2017, **27**, 1702018.
43 B. Wu, S.-T. Lu, H. Yu, R.-F. Liao, H. Li, B. L. Zafitatsimo, Y.-S. Li, Y. Zhang, X.-L. Zhu and H.-G. Liu, *Biomaterials*, 2018, **159**, 37–47.
44 T. Chen, D. Cen, Z. Ren, Y. Wang, X. Cai, J. Huang, L. Di Silvio, X. Li and G. Han, *Biomaterials*, 2019, **221**, 119419.
45 M. Abrigo, S. L. McArthur and P. Kingshott, *Macromol. Biosci.*, 2014, **14**, 772–792.
46 A. Chanda, J. Adhikari, A. Ghosh, S. R. Chowdhury, S. Thomas, P. Datta and P. Saha, *Int. J. Biol. Macromol.*, 2018, **116**, 774–785.
47 R. Qi, R. Guo, F. Zheng, H. Liu, J. Yu and X. Shi, *Colloids Surf., B*, 2013, **110**, 148–155.
48 R. Wang, L. Mu, Y. Bao, H. Lin, T. Ji, Y. Shi, J. Zhu and W. Wu, *Adv. Mater.*, 2020, **32**, 2002878.
49 L. Fan, H. Yang, J. Yang, M. Peng and J. Hu, *Carbohydr. Polym.*, 2016, **146**, 427–434.
50 Z. Ahmadian, A. Correia, M. Hasany, P. Figueiredo, F. Dobakhti, M. R. Eskandari, S. H. Hosseini, R. Abiri, S. Khorshid and J. Hirvonen, *Adv. Healthcare Mater.*, 2021, **10**, 2001122.
51 A. Dolgormaa, C.-j Lv, Y. Li, J. Yang, J.-x Yang, P. Chen, H.-p Wang and J. Huang, *Molecules*, 2018, **23**, 2982.
52 A. M. Sajjan, M. L. Naik, A. S. Kulkarni, U. F.-E.-H. Rudgi, M. Ashwini, G. G. Shirnalli, A. Sharanappa and P. B. Kalahal, *Chem. Data Collect.*, 2020, **26**, 100338.
53 S. Kim, H. Lim, S. Kim and D. Y. Lee, *J. Biomed. Eng. Res.*, 2020, **41**, 1–7.
54 G. Ma, N. Sun, Q. Yu, L. Han, L. Wu, H. Cao and G. Han, *Food Anal. Methods*, 2018, **11**, 415–425.
55 E. Y. Shin, J. H. Park, M. E. Shin, J. E. Song, M. Thangavelu, C. Carlomagno, A. Motta, C. Migliaresi and G. Khang, *Mater. Sci. Eng., C*, 2019, **103**, 109787.
56 B. Lu, M. Yi, S. Hu, D. Wu, Z. Zhu, C. Wu, Z. Wang, Y. Li and J. Zhang, *ACS Sustainable Chem, Eng.*, 2021, **9**, 5991–6000.
57 S. Jiang, K. Zhou, Y. Shi, S. Lo, H. Xu, Y. Hu and Z. Gui, *Appl. Surf. Sci.*, 2014, **290**, 313–319.
58 Z. Xiao, C. Xu, X. Jiang, W. Zhang, Y. Peng, R. Zou, X. Huang, Q. Liu, Z. Qin and J. Hu, *Nano Res.*, 2016, **9**, 1934–1947.
59 N. Karmaker, F. Islam, M. N. Islam, M. Razzak, F. A. Koly, A. S. Chowdhury and R. A. Khan, *J. Res. Updates Polym. Sci.*, 2019, **8**, 7–14.
60 M. Kariminejad, E. Sadeghi, M. Rouhi, R. Mohammadi, F. Askari, M. Taghizadeh and S. Moradi, *J. Food Process Eng.*, 2018, **41**, e12817.
61 H. Pan, Y. Yu, L. Li, B. Liu and Y. Liu, *Nanoscale Res. Lett.*, 2021, **16**, 84.
62 S. Wu, J. Hu, L. Wei, Y. Du, X. Shi and L. Zhang, *Food Chem.*, 2014, **148**, 196–203.
63 S. Ahn, C. O. Chantre, A. R. Gannon, J. U. Lind, P. H. Campbell, T. Grevesse, B. B. O'Connor and K. K. Parker, *Adv. Healthcare Mater.*, 2018, **7**, 1701175.
64 S. Ahmadian, M. Ghorbani and F. Mahmoodzadeh, *Int. J. Biol. Macromol.*, 2020, **162**, 1555–1565.
65 F. Mahmoudi Beram, G. A. Koohmareh and A. Malekpour, *Soft Mater.*, 2019, **17**, 41–56.
66 S. Khaledian, D. Kahrizi, S. T. J. Balaky, E. Arkan, M. Abdoli and F. Martinez, *J. Mol. Liq.*, 2021, **334**, 115989.
67 M. Adeli-Sardou, M. M. Yaghoobi, M. Torkzadeh-Mahani and M. Dodel, *Int. J. Biol. Macromol.*, 2019, **124**, 478–491.
68 A. Asiri, S. Saidin, M. H. Sani and R. H. Al-Ashwal, *Sci. Rep.*, 2021, **11**, 5634.
69 R. Rajasekaran, V. S. Seesala, K. C. Sunka, P. G. Ray, B. Saha, M. Banerjee and S. Dhara, *Mater. Sci. Eng., C*, 2020, **107**, 110218.
70 A. Balaji, S. K. Jaganathan, A. F. Ismail and R. Rajasekar, *Int. J. Nanomed.*, 2016, 4339–4355.
71 S. Ullah, M. Hashmi, J. Shi and I. S. Kim, *Polymers*, 2023, **15**, 2538.
72 H. Samadian, S. Farzamfar, A. Vaez, A. Ehterami, A. Bit, M. Alam, A. Goodarzi, G. Darya and M. Salehi, *Sci. Rep.*, 2020, **10**, 13366.
73 E. Hadipour-Goudarzi, N. Hemmatinejad and M. A. Shokrgozar, *Macromol. Mater. Eng.*, 2023, **308**, 2200562.
74 M.-A. Shahbazi, P. V. Almeida, E. M. Mäkilä, M. H. Kaasalainen, J. J. Salonen, J. T. Hirvonen and H. A. Santos, *Biomaterials*, 2014, **35**, 7488–7500.
75 H. Chhabra, P. Gupta, P. J. Verma, S. Jadhav and J. R. Bellare, *Mater. Sci. Eng., C*, 2014, **37**, 184–194.
76 M. H. A. Elella, R. R. Mohamed and M. W. Sabaa, *Carbohydr. Polym.*, 2018, **189**, 107–114.
77 J. Hafsa, M. A. Chaouch, B. Charfeddine, C. Rihouey, K. Limem, D. Le Cerf, S. Rouatbi and H. Majdoub, *Pharm. Biol.*, 2017, **55**, 156–163.

78 J. Carneiro, P. M. Döll-Boscardin, B. C. Fiorin, J. M. Nadal, P. V. Farago and J. P. D. Paula, *Braz. J. Pharm. Sci.*, 2016, **52**, 645–651.
79 H. Wu, H. Shi, Y. Wang, X. Jia, C. Tang, J. Zhang and S. Yang, *Carbon*, 2014, **69**, 379–389.
80 N. Sakthiguru and M. A. Sithique, *Int. J. Biol. Macromol.*, 2020, **152**, 873–883.
81 E. Marugan, E. P. Rebitski, M. Darder, S. R. Balestra, G. del Real and P. Aranda, *Appl. Clay Sci.*, 2023, **241**, 107002.
82 M. Chelu, M. Popa, E. A. Ozon, J. Pandele Cusu, M. Anastasescu, V. A. Surdu, J. Calderon Moreno and A. M. Musuc, *Polymers*, 2023, **15**, 1312.
83 M. R. Zare, M. Khorram, S. Barzegar, B. Sarkari, Q. Asgari, S. Ahadian and K. Zomorodian, *Int. J. Biol. Macromol.*, 2021, **182**, 1310–1321.
84 S. Gao, W. Zhang, X. Zhai, X. Zhao, J. Wang, J. Weng, J. Li and X. Chen, *Biomater. Sci.*, 2023, **11**, 533–541.
85 B. Yang, Y. Dong, Y. Shen, A. Hou, G. Quan, X. Pan and C. Wu, *Bioactive Materials*, 2021, **6**, 2400–2411.
86 B. Z. Chen, L. Q. Zhang, Y. Y. Xia, X. P. Zhang and X. D. Guo, *Sci. Adv.*, 2020, **6**, eaba7260.
87 L. Zhao, L. K. Vora, S. A. Kelly, L. Li, E. Larraneta, H. O. McCarthy and R. F. Donnelly, *J. Controlled Release*, 2023, **356**, 196–204.
88 L. K. Vora, R. F. Donnelly, E. Larrañeta, P. González-Vázquez, R. R. S. Thakur and P. R. Vavia, *J. Controlled Release*, 2017, **265**, 93–101.
89 Y. Xie, H. Wang, J. Mao, Y. Li, M. Hussain, J. Zhu, Y. Li, L. Zhang, J. Tao and J. Zhu, *J. Mater. Chem. B*, 2019, **7**, 6604–6611.
90 M. C. Lobita, N. El-Sayed, J. F. Pinto and H. A. Santos, *Int. J. Pharm.*, 2023, **642**, 123143.
91 J. He, Y. Liang, M. Shi and B. Guo, *Chem. Eng. J.*, 2020, **385**, 123464.
92 A. Wali, M. Gorain, S. Inamdar, G. Kundu and M. Badiger, *ACS Applied Bio Materials*, 2019, **2**, 4324–4334.
93 K. M. Rao, K. Sudhakar, M. Suneetha, S. Y. Won and S. S. Han, *Int. J. Biol. Macromol.*, 2021, **190**, 792–800.
94 S. Hashemikia, F. Farhangpazhouh, M. Parsa, M. Hasan, A. Hassanzadeh and M. Hamidi, *Int. J. Pharm.*, 2021, **597**, 120313.
95 S. Lohrasbi, E. Mirzaei, A. Karimizade, S. Takallu and A. Rezaei, *Cellulose*, 2020, **27**, 927–940.
96 F. Kalalinia, Z. Taherzadeh, N. Jirofti, N. Amiri, N. Foroghinia, M. Beheshti, B. S. F. Bazzaz, M. Hashemi, A. Shahroodi and E. Pishavar, *Int. J. Biol. Macromol.*, 2021, **177**, 100–110.
97 M. Hajikhani, Z. Emam-Djomeh and G. Askari, *Int. J. Biol. Macromol.*, 2021, **172**, 143–153.
98 B. Zhang, J. He, M. Shi, Y. Liang and B. Guo, *Chem. Eng. J.*, 2020, **400**, 125994.
99 Y. Liang, X. Zhao, T. Hu, B. Chen, Z. Yin, P. X. Ma and B. Guo, *Small*, 2019, **15**, 1900046.
100 W.-N. Wang, P. Pei, Z.-Y. Chu, B.-J. Chen, H.-S. Qian, Z.-B. Zha, W. Zhou, T. Liu, M. Shao and H. Wang, *Chem. Eng. J.*, 2020, **397**, 125488.
101 L. Hong, X. Liu, L. Tan, Z. Cui, X. Yang, Y. Liang, Z. Li, S. Zhu, Y. Zheng and K. W. K. Yeung, *Adv. Healthcare Mater.*, 2019, **8**, 1900835.
102 Z. Yang, R. Huang, B. Zheng, W. Guo, C. Li, W. He, Y. Wei, Y. Du, H. Wang and D. Wu, *Adv. Sci.*, 2021, **8**, 2003627.
103 V. Nosrati-Siahmazgi, S. Abbaszadeh, K. Musaie, M. R. Eskandari, S. Rezaei, B. Xiao, F. Ghorbani-Bidkorpeh and M.-A. Shahbazi, *Mater. Today Bio*, 2024, **26**, 101062.
104 K. Musaie, S. Abbaszadeh, V. Nosrati-Siahmazgi, M. Qahremani, S. Wang, M. R. Eskandari, S. V. Niknezhad, F. Haghi, Y. Li and B. Xiao, *Biomater. Sci.*, 2023, **11**, 2486–2503.